Morphology of sol-gel porous In-Ga-Zn-O thin films as a function of annealing temperatures

Christine Revenant, Mohammed Benwadih

Morphology of Sol-Gel Porous In-Ga-Zn-O Thin Films as a function of Annealing Temperatures

Christine Revenant,[a,b,*] Mohammed Benwadih[c,d]

[a]Univ. Grenoble Alpes, INAC-MEM, F-38000 Grenoble, France

[b]CEA, INAC-MEM, F-38000 Grenoble, France

[c]Univ. Grenoble Alpes, LITEN, F-38000 Grenoble, France

[d]CEA, LITEN, F-38000 Grenoble, France

Corresponding Author

*christine.revenant@cea.fr

CEA, INAC

17 rue des Martyrs

F-38054 Grenoble Cedex 9, France

Abstract

The physics of solution-processed thin films is studied with the example of In-Ga-Zn-O. After annealing at 450°C, the films become fully inorganic and the pore distribution is modeled by a hexagonal close-packed based structure. The surface porosity is approximately 0.23 and the volume porosity deduced from small-angle x-ray scattering is approximately 0.26. The corresponding specific surface area is in the range of 65 m^2g^{-1}. An instability model allows to successfully describe the film morphology. The solution diffusion coefficient, estimated from the rate of thinning as a function of temperature, follows an Arrhenius behavior with an activation energy of approximately 9.1×10^3 $Jmol^{-1}$ and a pre-exponential coefficient D_0 of approximately 1.8×10^{-8} m^2s^{-1}. Moreover, the surface tension-to-viscosity ratio of the solution is determined from the surface morphology. In addition, the observed phase separation between ZnO and Ga_2O_3 may come from the solubility difference of these oxides in the solvent. This separation has a major consequence on the electronic material properties. Finally, during cooling, the large tensile stress occurring between the film and the substrate is relaxed by the pores which adopt an oblate spheroid shape. The surface energy of In-Ga-Zn-O is then estimated to 1.5 Jm^{-2} from the pressure on the spheroidal pore.

Keywords: sol-gel; thin films; porosity; diffusion; solubility; phase separation

1. Introduction

Sol-gel for thin film fabrication is an important practical process [1]. Indeed, solvent extraction is one of the most used technological processes. “The ability to control the degree of shrinkage during drying is critical for many potential applications ranging from advanced thermal insulation (where no shrinkage is desirable) to optical films (where shrinkage is desired to control the porosity and hence the refractive index) to microporous adsorbents and membranes (where large shrinkage is desirable to produce small pores)” [2].

Periodic surface tension differences caused by concentration or/and temperature gradients produce a regular surface pattern. This phenomenon called Marangoni instability is a surface tension-driven interfacial convection, which generates regular vortices and thickness differences in the layer. Mesoscopic self-organization of Marangoni-like surface tension instabilities were related under intensive evaporation [3]. A convective instability due to concentration gradients was proposed in films elaborated with volatile solvent [4].

Despite a tremendous use of sol-gel thin films, there has been relatively little effort directed toward understanding the fundamental physics of sol-gel thin films. Here, we consider In-Ga-Zn-O (IGZO) thin films elaborated by sol-gel. Such transparent conducting oxide plays a critical role in the fabrication of many current and emerging optoelectronic devices. The films were thoroughly characterized by microscopy, small-angle x-ray scattering and x-ray absorption spectroscopy [5,6]. We put in evidence that the films are spatially heterogeneous. First, pores at the film surface and also inside the film appear after annealing above 300°C. The pores, produced by the evaporation of residual organics, have an oblate spheroid shape with an aspect ratio of 0.7. Second, the Zn and Ga environments are short-range ordered. The Ga atoms are in a

β-Ga_2O_3 like structure, mostly tetrahedral gallium oxide phase. The Zn atoms are in a tetrahedral ZnO phase. The size of these phases was estimated to 4-6 nm. The nanoclusters of ZnO and Ga_2O_3 are self-organized. The Ga_2O_3 nanoclusters decorate the pores, as the ZnO nanoclusters are in between. According to thermogravimetric analysis (TGA) measurements, the thermal removal of the organic compounds is complete at around 450°C [7].

In the present paper, we link the morphological observations to a convective instability due to concentration gradients in the film and obtain fundamental parameters of the sol-gel films. Our approach provides an important clue to understanding the morphology of IGZO thin films but also, more generally, solution-processed films.

2. Experimental

The IGZO precursor solution was prepared by dissolving organo-metallic zinc oximates [8,9], indium oximates [10], and gallium oximates in 2-methoxyethanol. The precursor decomposition pathway for zinc oxide was described by J. J. Schneider et al [8]. The water is released first, then the products from the organic ligands are liberated. The chemical composition ratio of IGZO precursor solution was In:Ga:Zn = 3:0.4:2 at a single layer concentration of 30 mg of precursor in a total of 1.0 g of solvent. The IGZO solution was deposited on a SiO_2 (100 nm)/Si substrate by spin coating. The sample was placed onto a hot plate for 10 min at different temperatures (200, or 300, or 380, or 450°C). It was then quench cooled to room temperature on a metal block for 30 s. The detailed preparation and characterization were previously published [5,6].

3. Results and discussions

3.1. Film thickness

During thermal annealing, the organic constituents evaporate and the film thickness decreases. The film thickness was measured from SEM cross-section images after thermal annealing at 300, 380 and 450°C [5]. The film thickness was measured from AFM cross-section images after thermal annealing at 200°C [11]. For the as-deposited film (20°C), the SEM beam would significantly evaporate the solution-based film and the AFM tip would sink in the film. In both cases, the thickness measurement would not be reliable. Hence, we resorted to estimating the as-deposited film thickness from the TGA data. The thickness ℓ_{20} of the deposited film at room temperature can be deduced, as the ratio between the film weight at 20°C (m_{20}) and that at 200°C (m_{200}) is known from TGA. The thickness ℓ_{20} can be calculated using:

$$\ell_{20} = \ell_{200} \times m_{20}/m_{200}. \quad (1)$$

We estimate the thickness of the deposited film ℓ_{20} to 67 nm. The decrease of the film thickness ℓ with temperature is reported in Figure 1.

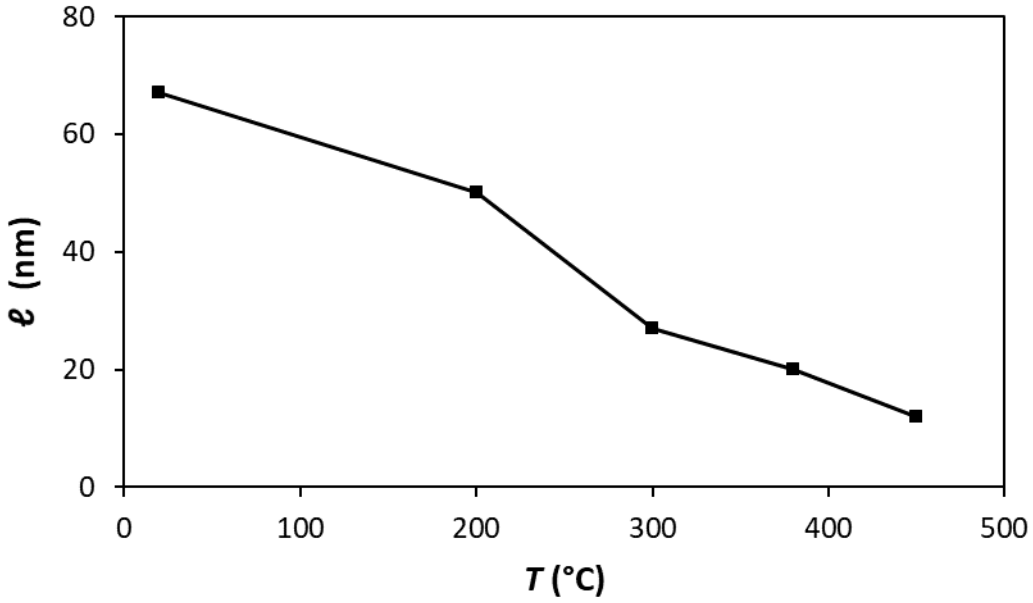

Figure 1. Thickness ℓ of the IGZO thin film vs the annealing temperature T. Line serves as a guide to the eye.

3.2. Surface porosity

Figure 2 displays a transmission electron microscopy (TEM) view of the IGZO surface annealed at 450°C. Nanometer-sized pores are regularly distributed at the film surface. The arrangement of the pores is close to a 2D hexagonal close-packed (hcp) structure. An analysis of the TEM image yields a surface porosity of approximately 0.23.

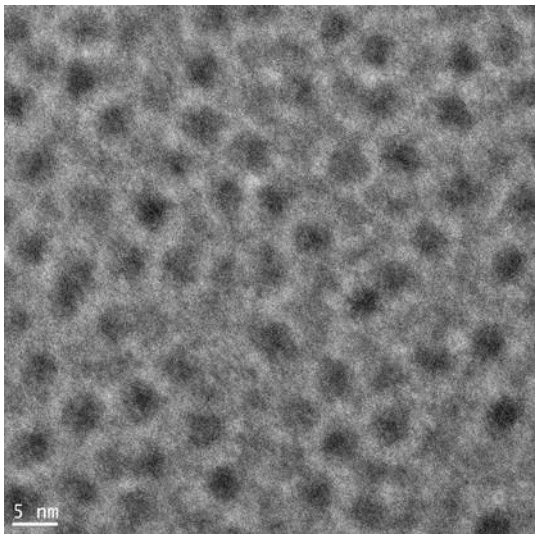

Figure 2. Plane-view TEM image of IGZO film annealed at 450°C. The black areas correspond to pores.

The pores have approximately a disk-shape section at the film surface. The area of a pore section is πr^2, where r is the pore radius at the surface. The area of the hexagon is $(3\sqrt{3})D^2/2$, where D is the distance between the centers of two adjacent pores. Then, with three pores by hexagon, the surface porosity ϕ_s is:

$$\phi_s = (2\pi/\sqrt{3})\,(r/D)^2 \qquad (2)$$

The surface porosity (Figure 3) increases as a function of the square of r/D.

At the maximum value of r/D=0.5 corresponding to the contact between neighboring pores, ϕ_s is maximum at $\pi/(2\sqrt{3})$ i.e. ~ 0.9. In our example, measurements indicated r=3 nm and D=12 nm for the film annealed at 450°C [5]. Hence, we have r/D=0.25 and a surface porosity ϕ_s of 0.23. This value is in excellent agreement with that found directly from the analysis of the microscopy image.

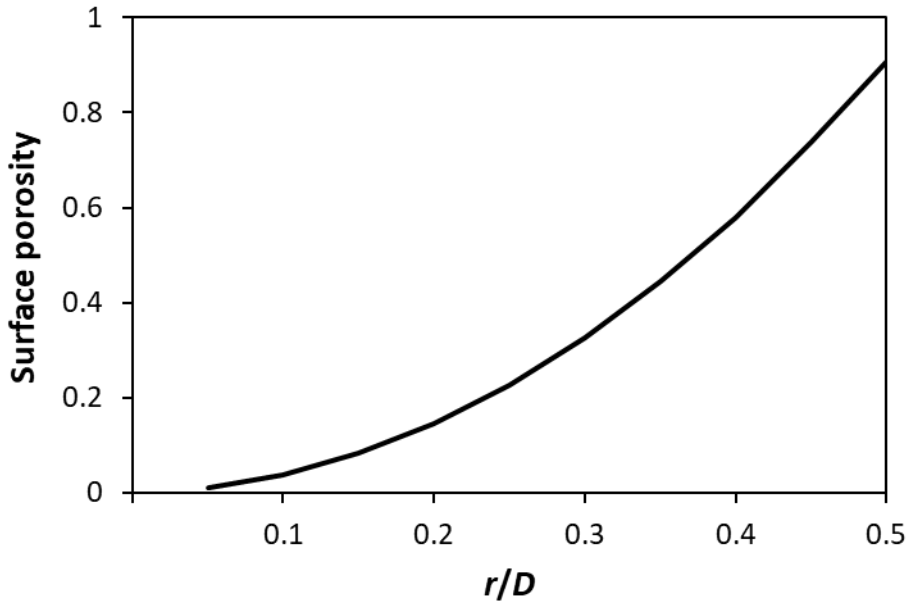

Figure 3. Surface porosity in a 2D hcp pore structure as a function of r/D. The pores have a radius r and are distant of D.

3.3. Volume porosity

Pores were put in evidence also inside the film by scanning transmission electron microscopy (STEM) and Grazing Incidence Small Angle X-ray Scattering (GISAXS) [5]. Presently, we model the film of thickness ℓ with pores arranged in an hcp-based cell with an in-plane (resp. out-of-plane) parameter D (resp. c). Each pore is modeled by an oblate spheroid of radius r and height h. The volume porosity can be expressed as:

$$\phi_V = (N_p \times V_p)/ V_{cell} \quad (3)$$

where N_p is the number of pores in the unit cell, V_p is the volume of each pore and V_{cell} is the volume occupied by the unit cell. In an hcp-based cell, N_p=6 and V_{cell}=$[(3\sqrt{3})/2]D^2c$. For spheroid pore, V_p=$(4/3)\pi r^2(h/2)$. We obtain:

$\phi_V = [8\pi/(3\sqrt{3})](r/D)^2(h/c)$ (4)

Combining eq 2 and 4, the volume porosity can be expressed as a function of the surface porosity:

$\phi_V = (4/3)\ \phi_S\ (h/c)$. (5)

The volume porosity can be different from the surface porosity. The volume porosity depends linearly of h/c. As $c \geq h$, $\phi_V \leq (4/3)\ \phi_S$. The volume porosity is smaller than 1.3 times the surface porosity. In our case r/D=0.25, we get:

$\phi_V = [\pi/(6\sqrt{3})](h/c)$ (6)

Then, the maximum of the volume porosity is $\phi_{Vmax} = \pi/(6\sqrt{3}) \sim 0.30$. Moreover, the volume porosity ϕ_V of the thin film can be expressed as:

$\phi_V = 1-(\rho/\rho_0)$ (7)

where ρ_0 is the bulk mass density of the material and ρ is the mass density of the porous thin film. In our case, $\rho_0 \sim$ 6.5 g.cm^{-3} for amorphous bulk IGZO with In/(In+Zn)=3/5=0.6 [12]. Hence, the maximum of the volume porosity is linked to the minimum of the mass density ρ_{min} of the porous thin film:

$\rho_{min} = \rho_0\ (1-\phi_{Vmax})$ (8)

In our case, we have $\rho_{min} \sim 0.7\rho_0 \sim$ 4.6 g.cm^{-3}.

We go further by using GISAXS in order to estimate the volume porosity. GISAXS is indeed a powerful technique to study the volume porosity [13]. The critical angle α_c for total external reflection corresponds to the Yoneda peak position in GISAXS and is related to the δ parameter by:

$$\alpha_c = \sqrt{2\delta} \tag{9}$$

In addition, δ is related to the atomic density ρ_a by [14]:

$$\delta = \frac{r_e \rho_a (\overline{Z+f'}) \lambda^2}{2\pi} \tag{10}$$

where r_e is the classical electron radius, Z is the number of electrons per atom, f' is the dispersion correction and λ is the X-ray wavelength. The atomic density ρ_a is related to the material density ρ by:

$$\rho_a = \frac{\rho N_A}{M} \tag{11}$$

where N_A is the Avogadro's number and M is the atomic or molecular weight. Finally, ρ can be expressed as:

$$\rho = \frac{\pi \alpha_c^2 \bar{M}}{r_e N_A (\overline{Z+f'}) \lambda^2}. \tag{12}$$

GISAXS measurements were performed at 9590 eV at beamline BM02 at ESRF, Grenoble, France and the GISAXS intensity was normalized with respect to the incident beam intensity. An intensity cut as a function of the out-of-plane angle α_f is taken at an in-plane angle $2\theta_f$ of 0.7 deg (corresponding to the interference peak maximum) with a cut width of 0.1 deg (Figure 4). The maximum of the cut gives a critical angle α_c of 0.165 deg for IGZO annealed at 450°C.

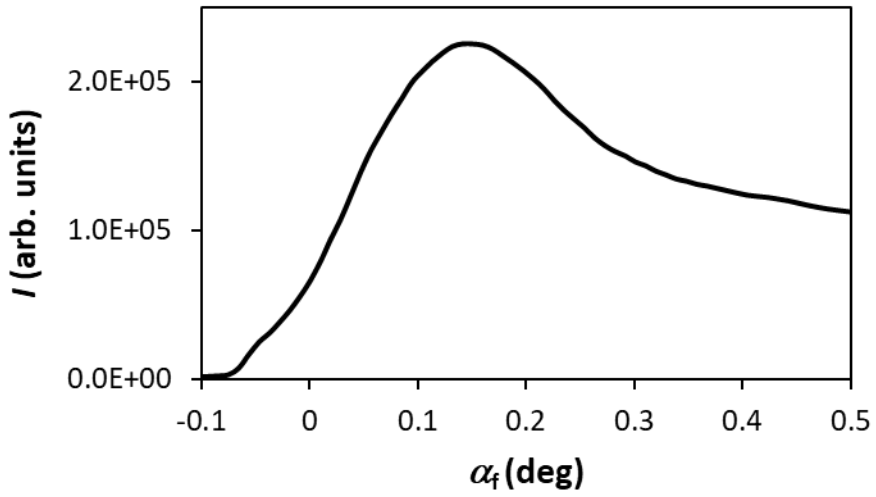

Figure 4. GISAXS intensity as a function of the out-of-plane angle α_f at an in-plane angle $2\theta_f$ of 0.7 deg with a cut width of 0.1 deg for IGZO annealed at 450°C.

Then, the calculation yields ρ=4.8 g.cm^{-3} for the film annealed at 450°C. This value is above ρ_{min} as expected. Finally, the experimental porosity of the film at 450°C is ϕ_V=1-(4.8/6.5)=0.26 which is similar to the surface porosity. Finally, from eq 6, one can get an estimate of h/c. We get h/c~0.9 and as $(h/2)/r \sim 0.7$, h~4.2 nm. Finally, c~4.7 nm. The pore distribution was modeled by an hcp-based model with an in-plane parameter D of 12 nm and an out-of-plane parameter c of 4.7 nm for the film at 450°C. The ratio c/D is equal to 0.4, indicating a tensile hcp structure.

Another important parameter to characterize mesoporous films is the specific surface area, as the structure and the properties of such films may be different at surfaces or inside the volume. The surface area of an oblate spheroid pore is:

$$S_s=2\pi r^2[1+((1-e^2)/e)\tanh^{-1}e] \quad (13)$$

where $e^2=1-[(h/2)^2/r^2]$

The specific surface S_p of pores in the hcp-based cell is given by:

$$S_p=N_p\times S_s/(\rho_0\times V_s), \quad (14)$$

where V_s is the volume of the solid phase.

$$V_s = V_{cell} - N_p\times V_p \quad (15)$$

In our case, e~0.7 and $S_s=1.6 \times 2\pi r^2$. At 450°C, the specific surface area S_s is as large as 65 m^2g^{-1}.

3.4. Diffusion coefficient

The pore patterning may be related to solute-capillary Marangoni flow or to the instability introduced by de Gennes (Figure 5) [4]. The volume fraction of solvent $\psi(z)$ varies from the bottom of the film (down fraction ψ_d) to the free surface (up fraction ψ_u). The diffusion current in the film (number of molecules per unit area and per second) is:

$$W = D_{coop} (\psi_d - \psi_u)/(a^3\ell) \quad (16)$$

where D_{coop} is the cooperative diffusion coefficient of the solution and a is the size of a solvent molecule.

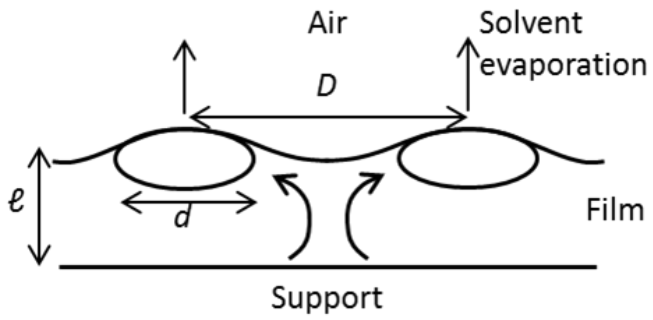

Figure 5. Scheme of the film of thickness ℓ. The hot fluid rises towards the cold surface and lowers the surface tension (low region). Thus the fluid is driven laterally (high region). Solvent-rich bubbles nucleate at the high region of the film. The distance between the bubbles is D and their diameter is d.

The rate of thinning depends on the flux W:

$$d\ell/dt=-a^3W \quad (17)$$

Using both equations, this gives an evaporation rate:

$$-(1/\ell)(d\ell/dt)=(D_{coop}/\ell^2)\,(\psi_d-\psi_u) \quad (18)$$

At low temperature annealing (200°C), TGA measurements indicate that there is a high concentration of solvent. Hence, $\psi_d\sim1$. The solvent at the surface evaporates ($\psi_u\sim0$). On the contrary, during high temperature annealing (380, 450°C), TGA measurements indicate that there is a low concentration of solvent. At one point, there is no solvent anymore at the bottom of the film ($\psi_d\sim0$) and the extra solvent coming from down still evaporates near the free surface ($\psi_u\sim1$). Hence, in both regimes, $|\psi_d-\psi_u|\sim1$. Then,

$$D_{coop}\sim \ell\,(d\ell/dt). \quad (19)$$

By using the average of the film thickness during annealing, the diffusion coefficient D_{coop} was estimated as a function of the annealing temperature (Table 1). The diffusion coefficient D_{coop} increases with the annealing temperature.

Table 1. Estimate of the diffusion coefficient of the solution as a function of the annealing temperature. The parameter $\langle \ell \rangle$ is the average of the film thickness during annealing.

T (°C)	200	380	450
$\langle \ell \rangle$ (nm)	59	44	40
$d\ell/dt$ (nm s^{-1})	0.028	0.078	0.092
D_{coop} (m^2s^{-1})	1.7×10^{-9}	3.4×10^{-9}	3.7×10^{-9}

The diffusion coefficient as a function of temperature T is described by the Arrhenius relation.

$$D_{coop} = D_0 e^{-Ea/RT} \qquad (20)$$

where E_a is the activation energy, D_0 is the pre-exponential coefficient and R is the gas constant. The diffusion data from Table 1 are fully compatible with an Arrhenius law (Figure 6). Linear fit of the data yields an activation energy of approximately 9.1×10^3 $Jmol^{-1}$ and a pre-exponential coefficient D_0 of approximately 1.8×10^{-8} m^2s^{-1}.

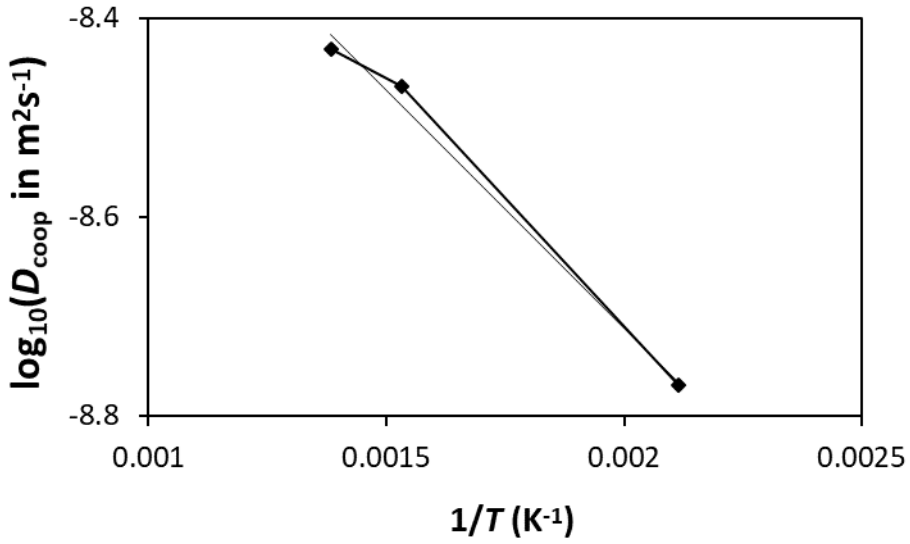

Figure 6. Arrhenius diagram of the diffusion coefficient. The curve with squares corresponds to the estimated diffusion coefficient of the solution. The thin line corresponds to the linear fit.

3.5. Characteristic velocity

Let us estimate the amplitude of the surface undulations when convection dominates over diffusion i.e. when the convective velocity is above a crossover value $V_1=D_{coop}/D$ [4]. The undulations correspond to a velocity field of magnitude V_1. The corresponding shear stress σ and scalar pressures p should then be:

$$\sigma \sim p \sim \eta\, V_1/\ell \sim \eta \times D_{coop}/(D\times\ell), \qquad (21)$$

where η is the solution viscosity. Within one "period" D, there is a high evaporation zone (undulation top) and a low evaporation zone (undulation bottom). Each region has a characteristic length of (D/2). The pore (diameter d) is situated in the undulation top. This convective behavior may explain why the pore diameter is approximately half

the distance between the pores. If the undulation amplitude is h_u, the curvatures are of order $h_u/(D/2)^2$. The corresponding Laplace pressure must be comparable to p:

$$p \sim 2\gamma\, h_u /(D/2)^2 \quad (22)$$

where γ is the surface tension.

$$V^* = (1/8)\,(D_{coop}/\ell)(D/h_u), \quad (23)$$

where $V^* = \gamma/\eta$ is the characteristic velocity [15]. The roughness of the film was measured by AFM [11]. The relation (23) can be used to obtain the characteristic velocity. At 380°C, D= 11 nm, h_u =2.6 nm, hence V^*=0.041 m.s^{-1}. At 450°C, D= 12 nm, h_u =2.2 nm, hence V^*=0.063 m.s^{-1}. The characteristic velocity of the solution is larger at 450°C than at 380°C indicating that the dynamics of the film is more strongly affected at 450°C than at 380°C. In comparison, the 2-methoxyethanol solvent has a surface tension γ =30.84 mN/m [16] and η = 1.7 mPa.s at room temperature leading a surface tension-to-viscosity ratio of approximately 18 m.s^{-1}. The solution characteristic velocity is approximately 400 (resp. 300) times smaller at 380°C (resp. 450°C) than that of the 2-methoxyethanol solvent at room temperature.

3.6. Phase separation

The real atomic composition of the IGZO films was estimated by XPS measurements. Figure 7 displays the In/Ga and Zn/Ga composition ratio as a function of the annealing temperature. The In/Ga ratio is in the range 4.6 - 6.3, as the Zn/Ga ratio is in the range 3.5 - 4.3 for the considered temperatures.

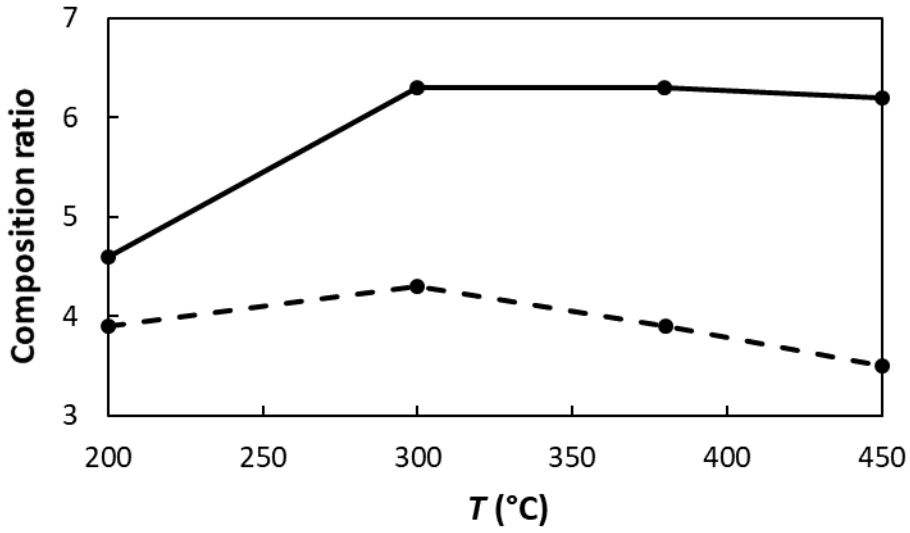

Figure 7. Estimate of the atomic composition ratio In/Ga (continuous line) and Zn/Ga (dotted line) of the IGZO film as a function of the annealing temperature.

Regarding indium, the XPS spectrum of In 3d has a peak centered at 444 eV characteristic of In-O [7]. In addition, energy dispersive X-ray spectroscopy (EDX) measurements show that indium oxide form clusters of a few nanometers (Figure 8).

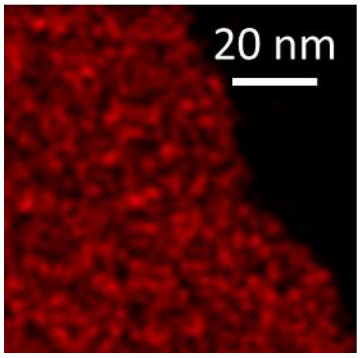

Figure 8. EDX elemental mapping of In.

Regarding the other metals, the zinc complexes were prepared according to the method of J. J. Schneider *et al.* [8] from zinc nitrates, as the gallium oximates were prepared with chlorides [6]. “In synthesizing the sol-gel-derived MOS precursor solutions using metal salts, metal chlorides have been commonly used as precursor

compounds, because they are easy to be formulated into solution-processable semiconductors due to their high solubilities in various solvents. Other precursors such as metal nitrate, acetate, and acetylacetonate are not very soluble in specific solvents with a molar concentration above 0.1 M and the solubility is improved by adding various chelation agents in a sophisticated manner" [17]. During annealing, the solvent with metal complexes move to the nucleation sites of the bubbles. During this motion, the ZnO progressively precipitates from the solvent, as it is not very soluble. On the contrary, Ga_2O_3 moves with the solvent to the nearest nucleation sites. In a second step, when the solvent evaporates, Ga_2O_3 remains at the pores (Figure 9)**.** It is considered that this mechanism creates the deposition of Ga_2O_3 around pores. To summarize, a poor solubility of ZnO in the solvent causes the first phase separation (ZnO/solvent). Then the solvent evaporation induces the phase separation for Ga_2O_3. The solubility difference between ZnO and Ga_2O_3 in the solvent is at the origin of ZnO and Ga_2O_3 separation. This solubility difference between ZnO and Ga_2O_3 in the solvent has a major consequence on the electronic properties of the IGZO semiconductor. As a matter of fact, x-ray absorption spectroscopy reveal that the Zn atoms localized at the nanocluster boundary are undercoordinated with O [6]. Such ZnO cluster boundary could be responsible for electronic defect levels that were put in evidence in the upper half of the band gap. If both metal oxides had similar solubility in the solvent, they would be deposited in similar regions. In case of poor solubility, they would be deposited in between the pores. In case of good solubility, they would be deposited at the pore walls.

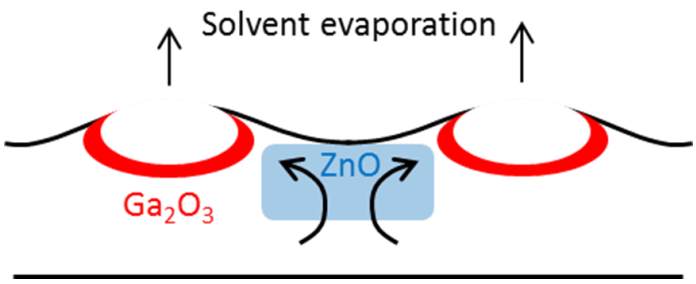

Figure 9. Schematic illustrating the separation between ZnO and Ga_2O_3. ZnO is deposited in the region between the pores. Ga_2O_3 is deposited at the pore walls as the solvent evaporates.

3.7. Surface energy

During annealing, the sol-gel layer adheres well to the substrate. On the contrary, during cooling from high temperature to room temperature, the layer is stiffer as it lost organic material. The linear thermal expansion coefficient of the SiO_2 substrate is α=0.40×10^{-6} K^{-1} at 300 K [18] and that of a-IGZO is estimated to be 1.6 × 10^{-5} K^{-1} [19]. The thermal expansion coefficient of IGZO is 40 times larger than that of SiO_2. During cooling, the IGZO layer tries to shrink, but the SiO_2 substrate restricts it from doing so. Hence, the IGZO layer is under tension. In pure IGZO films, the film contraction could only be macroscopically relaxed in the direction normal to the substrate. On the contrary, in mesostructured films, the stress may be locally relaxed by the deformation of the mesopores. The tensile stress is relaxed by the pores which adopt an oblate spheroid shape. In case of a gas particle in a homogeneous medium, the energy is minimum when the surface is minimum. Other examples of ellipsoidal pores in amorphous metal-oxide-based films can be found in the literature. Boissiere et al. put in evidence that, during annealing of the films, the contraction of the mesostructure yields to an ellipsoidal contraction of pores [20]. Similarly, Kuemmel et al. studied the

pore shape in γ-Al_2O_3 nanocrystallized mesoporous film. The pores are ellipsoidal with a large anisotropy due to the high degree of contraction induced by the thermal treatment [21]. The stress between the layer and the substrate is dominated by the thermal contraction difference, according to

$$\sigma=(E/(1-v))\,(\alpha_s-\alpha_l)\,\Delta T \quad (24)$$

where α_s, α_l refer to the linear thermal expansion coefficient of the substrate and the layer respectively, $E/(1-v)$ is the biaxial modulus of the layer, v is the Poisson's ratio, and E is the Young modulus [22]. The Young modulus of IGZO was estimated to 130 GPa [23]. No direct measurement of Poisson's ratio for IGZO was found in literature. However, the Poisson's ratio of ZnO is 0.36 [24] and that of another transparent conducting oxide ITO thin film is 0.35 [25]. So, we use this value for Poisson's ratio of IGZO. Finally, for T=450°C, we find σ=-1.34 GPa. The corresponding Laplace pressure on the ellipsoidal pore during cooling is

$$P=\gamma\times[(r/(h/2)^2)+((h/2)/r^2)]. \quad (25)$$

Using both relations (24) and (25), we obtain: γ~1.5 Jm^{-2} for IGZO after an annealing at 450°C. Surface energies of oxides are mostly in the range 0.5-3.5 Jm^{-2} [26]. Relaxed surface energies of In_2O_3 are 1.76 Jm^{-2} for (100), 1.07 Jm^{-2} for (110), and 0.89 Jm^{-2} for (111) surface [27]. Anhydrous surface of wurtzite ZnO has surface energies of 2.55 Jm^{-2} [28]. Surface energies for relaxed β-Ga_2O_3 is in the range of 0.68-2.03 Jm^{-2} according to the orientation and reconstruction of the surface [29]. So, the obtained γ value is in good agreement with those of close oxides.

4. Conclusions

The morphological properties of mesoporous IGZO thin films were studied. A concentration-driven instability well describes the roughness and the porosity of the film. Structural data were used to derive fundamental quantities, like the diffusion coefficient of the solution and the oxide surface energy. Tailoring porosity in sol-gel thin films could be achieved by varying the characteristic velocity i.e. the solution viscosity and the surface tension. The phase separation between ZnO and Ga_2O_3 has its origin in a solubility difference of these compounds in the solvent. The coating of the pores by Ga_2O_3 comes first from the motion of this oxide up to the bubble and second from the solvent evaporation. The solubility difference between both metal oxides in the solvent is responsible for electronic defect levels. Hence, similar preparation of metal oximates should be favored as far as possible. This new insight is of uttermost importance for future chemistry research in solution-processing. The oblate shape of the pores is explained by the thermal-induced tensile stress of the layer during cooling. Although the drying-shrinkage model was illustrated for IGZO thin films, the here-detailed analysis is applicable to other porous thin films and solvents. With the knowledge of fundamental parameters, it is possible to rationalize the morphology of sol-gel thin films and ultimately to control the properties.

Acknowledgements

We thank C. Serbutoviez for discussions, K. Bonrad and A. Klyszcz from Merck KGaA for supplying the IGZO solution, M. Maret, N. Boudet, N. Blanc, and the technical staff of BM2 for assistance during the GISAXS experiments. We acknowledge the French CRG committee for provision of synchrotron radiation beamtime.

References

[1] C. J. Brinker, A. J. Hurd, P. R. Schunk, G. C. Frye, C. S. Ashley, Review of Sol-Gel Thin Film Formation, Journal of Non-Crystalline Solids 147&148 (1992) 424-436.

[2] D.M. Smith, G.W. Scherer, J.M. Anderson, Journal of Non-Crystalline Solids 188 (1995) 191-206.

[3] L. Weh, Surface Structures in Thin Polymer Layers Caused by Coupling of Diffusion-Controlled Marangoni Instability and Local Horizontal Temperature Gradient, Macromol. Mater. Eng. 290 (2005) 976-986.

[4] P. G. de Gennes, Instabilities during the Evaporation of a Film: Non-Glassy Polymer + Volatile Solvent, Eur. Phys. J. E 6 (2001) 421-424.

[5] C. Revenant, M. Benwadih, M. Maret, Self-Organized Nanoclusters in Solution-Processed Mesoporous In-Ga-Zn-O Thin Films, Chem. Commun. 51 (2015) 1218-1221.

[6] C. Revenant, M. Benwadih, O. Proux, Local Structure around Zn and Ga in Solution-Processed In-Ga-Zn-O and Implications for Electronic Properties, Phys. Status Solidi RRL 9 (2015) 652-655.

[7] M. Benwadih, J. A.Chroboczek, G. Ghibaudo, R. Coppard, D. Vuillaume, Impact of Dopant Species on the Interfacial Trap Density and Mobility in Amorphous In-X-Zn-O Solution-Processed Thin-Film Transistors, J. Appl. Phys. 115 (2014) 214501.

[8] J. J. Schneider, R. C. Hoffmann, J. Engstler, S. Dilfer, A. Klyszcz, E. Erdem; P. Jakes, R. A. Eichel, Zinc Oxide Derived from Single Source Precursor Chemistry

under Chimie Douce Conditions: Formation Pathway, Defect Chemistry and Possible Applications in Thin Film Printing, J. Mater. Chem. 19 (2009) 1449-1457.

[9] R. Kuegler, J. Schneider, R. Hoffmann, Organometallic Zinc Compound for Preparing Zinc Oxide Films, Patent No. WO/2009/010142, 2009.

[10] R. C. Hoffmann, M. Kaloumenos, S. Heinschke, E. Erdem, P. Jakes, R.-A. Eichel, J. J. Schneider, Molecular Precursor Derived and Solution Processed Indium-Zinc Oxide as a Semiconductor in a Field-Effect Transistor Device. Towards an Improved Understanding of Semiconductor Film Composition, J. Mater. Chem. C 1 (2013) 2577-2584.

[11] M. Benwadih, PhD thesis, University of Lille, France, 2014.

[12] A. C. Galca, G. Socol, V. Craciun, Optical Properties of Amorphous-like Indium Zinc Oxide and Indium Gallium Zinc Oxide Thin Films, Thin Solid Films 520 (2012) 4722-4725.

[13] M. Rawolle, M. A. Ruderer,; S. M. Prams, Q. Zhong, D. Magerl, J. Perlich, S. V. Roth, P. Lellig, J. S. Gutmann, P. Müller-Buschbaum, Nanostructuring of Titania Thin Films by a Combination of Microfluidics and Block-Copolymer-Based Sol-Gel Templating, Small 7 (2011) 884-891.

[14] G. Renaud, R. Lazzari, F. Leroy, Probing Surface and Interface Morphology with Grazing Incidence Small Angle X-Ray Scattering, Surface Science Reports 64 (2009) 255-380.

[15] K. Murata, H. Asakawa, K. Nagashima, Y. Furukawa and G. Sazaki, Insitu determination of Surface Tension-to-Shear Viscosity Ratio for Quasiliquid Layers on Ice Crystal Surfaces, Phys. Rev. Lett. 115 (2015) 256103.

[16] W. M. Haynes, CRC Handbook of Chemistry and Physics, 94th Edition, CRC Press LLC, Boca Raton: FL 2013-2014, p. 6-183.

[17] S. Jeong, J.-Y. Lee, S. S. Lee, Y. Choi, B.-H. Ryu, Impact of Metal Salt Precursor on Low-Temperature Annealed Solution-Derived Ga-doped In_2O_3 Semiconductor for Thin-Film Transistors, J. Phys. Chem C 115 (2011) 11773-11780.

[18] G. K. White, Thermal Expansion of Reference Materials: Copper, Silica and Silica, J. Phys. D: Appl. Phys. 6 (1973) 2070-2078.

[19] K. Ide, K. Nomura, H. Hiramatsu, T. Kamiya, H. Hosono, Structural Relaxation in Amorphous Oxide Semiconductor, a-In-Ga-Zn-O. J. Appl. Phys. 111 (2012) 073513.

[20] C. Boissiere, D. Grosso, S. Lepoutre, L. Nicole, A. Brunet Bruneau, C. Sanchez, Porosity and Mechanical Properties of Mesoporous Thin Films Assessed by Environmental Ellipsometric Porosimetry, Langmuir 21 (2005) 12362-12371.

[21] M. Kuemmel, D. Grosso, C. Boissiere, B. Smarsly, T. Brezesinski, P. A. Albouy, H. Amenitsch, C. Sanchez, Thermally Stable Nanocrystalline γ-Alumina Layers with Highly Ordered 3D Mesoporosity, Angew. Chem. Int. Ed. 44 (2005) 4589-4592.

[22] B. Wang, Z. Xiao, A Constitutive Equation for Viscoelastic Porous Gels during Syneresis and Drying, Mechanics of Materials 34 (2002) 299-311.

[23] T. Yoshikawa, T. Yagi, N. Oka, J. Jia, Y. Yamashita, K. Hattori, Y. Seino, N. Taketoshi, T. Baba, Y. Shigesato, Thermal Conductivity of Amorphous Indium-Gallium-Zinc Oxide Thin Films, Appl. Phys. Express 6 (2013) 021101.

[24] G. G. Gadzhiev, The Thermal and Elastic Properties of Zinc Oxide-Based Ceramics at High Temperatures, High Temperature 41 (2003) 778-782.

[25] D. G Neerinck, T. J. Vink, Depth Profiling of Thin ITO Films by Grazing Incidence X-Ray Diffraction, Thin Solid Films, 278 (1996) 12-17.

[26] A. Navrotsky, Nanoscale Effects on Thermodynamics and Phase Equilibria in Oxide Systems, ChemPhysChem 12 (2011) 2207-2215.

[27] K. H. L. Zhang, A. Walsh, C. R. A. Catlow, V. K. Lazarov, R. G. Egdell, Surface Energies Control the Self-Organization of Oriented In_2O_3 Nanostructures on Cubic Zirconia, Nano Lett. 10 (2010) 3740-3746.

[28] P. Zhang, F. Xu, A. Navrotsky, J. S. Lee; S. Kim, J. Liu, Surface Enthalpies of Nanophase ZnO with Different Morphologies, Chem. Mater. 19 (2007) 5687-5693.

[29] V. M. Bermudez, The Structure of Low-index Surfaces of β-Ga_2O_3, Chem. Phys., 323 (2006) 193-203.